Edinburgh Research Explorer

Finite element modeling of melting and fluid flow in the laser-heated diamond-anvil

OPEN ACCESS

Finite element modeling of melting and fluid flow in the laser-heated diamond-anvil cell

N. Gomez-Perez,[1,2,a)] J. F. Rodriguez,[3] and R. S. McWilliams[2,4,b)]

[1)]*Departamento de Geociencias, Universidad de los Andes. Bogotá,*

Colombia

[2)]*School of Physics and Astronomy and Centre for Science at Extreme Conditions,*

University of Edinburgh, Peter Guthrie Tait Road, Edinburgh,

UK EH9 3FD

[3)]*Departamento de Física, Universidad de los Andes. Bogotá,*

Colombia

[4)]*Geophysical Laboratory, Carnegie Institution of Washington,*

5251 Broad Branch Road NW Washington D.C. 20015

(Dated: 6 March 2017)

The laser-heated diamond anvil cell is widely used in the laboratory study of materials behavior at high-pressure and high-temperature, including melting curves and liquid properties at extreme conditions. Laser heating in the diamond cell has long been associated with fluid-like motion in samples, which is routinely used to determine melting points and is often described as convective in appearance. However, the flow behavior of this system is poorly understood. A quantitative treatment of melting and flow in the laser-heated diamond anvil cell is developed here to physically relate experimental motion to properties of interest, including melting points and viscosity. Numerical finite-element models are used to characterize the temperature distribution, melting, buoyancy, and resulting natural convection in samples. We find that continuous fluid motion in experiments can be explained most readily by natural convection. Fluid velocities, peaking near values of microns per second for plausible viscosities, are sufficiently fast to be detected experimentally, lending support to the use of convective motion as a criterion for melting. Convection depends on the physical properties of the melt and the sample geometry, and is too sluggish to detect for viscosities significantly above that of water at ambient conditions, implying an upper bound on the melt viscosity of about 1 mPa s when convective motion is detected. A simple analytical relationship between melt viscosity and velocity suggests direct viscosity measurements can be made from flow speeds, given basic thermodynamic and geometric parameters of samples are known.

[a] Electronic mail: ngomez@uniandes.edu.co

[b] Electronic mail: rs.mcwilliams@ed.ac.uk

I.   INTRODUCTION

Accurate experimental constraints on melting points and liquid properties in materials under high pressure conditions are needed in fields ranging from condensed matter theory[1,2] to planetary science[3–5], where high-pressure melts play a central role in magmatism, thermal evolution, and magnetic field generation. For most materials the melting temperature increases significantly under pressure. This includes fluids such as water[6] or hydrogen[7] which solidify under pressure, and solids such as iron[3,4,8–10] which exhibit significantly elevated melting points. It is thus necessary to reach temperatures on the order of thousands of degrees Kelvin in experiments at pressures of tens to hundreds of GPa to study melting and the properties of fluid phases.

The diamond anvil cell (DAC) has been an instrument of unparalleled utility in the laboratory study of matter at high pressure and temperature. Studies using this device have paid special attention to the characterization of phase transitions, and in particular, to melting. External heating of the DAC using resistive heating can reach temperatures of roughly $1000\,\mathrm{K}$ in samples, below melting temperatures for many materials under pressure. In contrast, laser heating of the diamond cell – i.e. localized, direct laser illumination of high pressure samples through the diamond optical window – can achieve maximum temperatures exceeding $10\,000\,\mathrm{K}$,[11,12] enough to melt all known materials to very high pressures.[1,4,5,13–17] This laser-assisted DAC setup is called the laser-heated diamond anvil cell (LHDAC).

While providing the capability of studying high-pressure melting and melts in virtually all substances, LHDAC techniques are often complicated, compared to homogeneous external heating, by very large standing temperature gradients in samples, on the order of hundreds to thousands of degrees K per micron.[9,10,12,18–31] Local pockets of melt can be stabilized in these temperature gradients, surrounded by lower-temperature solid matter and the cold, heat-sinking diamond anvils. The accurate detection of melting in such experiments is a longstanding challenge in high-pressure research. There is also a pressing need to determine the properties of the fluid state, including viscosity.

Among the most common[3,8–10,19,32–41] and controversial[1,4,14–17,42–44] diagnostics of melting in LHDAC experiments is the visual observation of motion in the laser-heated sample, which is attributed to fluid flow and often described as being 'convective' and 'continuous' in appearance.[3,9,32,34,36–42] While this motion is readily observable in experiments, there is

3

limited understanding of the nature and origin of the motion, and thus how it is connected to melting in the LHDAC. Sample motion has been usually characterized by qualitative criteria,[3,9,10,19,32,34,36–40,42] adding significant uncertainty to experimental interpretations. If, as qualitatively assessed, observed motions are convective in nature, then it stands to reason that these motions, coupled to information about temperature gradients and sample geometry, will enable assessment of fluid transport properties, and in particular viscosity. This information is also needed to assess systematic differences between melting studies. Motion-based criteria have yielded melting curves consistent with other approaches in many cases, for example in bridgmanite[32,42,45], sodium chloride[14,33] and aluminum[1] but pronounced and as-yet unresolved discrepancies in others, as in iron[3,4], tantalum[16,35,44] and molybdenum.[15,35] In this study we address this gap in knowledge by quantitatively relating melting and motion in the LHDAC, establishing its underlying physical basis and assessing possible observable phenomena in experiments which may signal the cause of the flow and the character of the fluid state.

In the past, order-of-magnitude considerations have been applied to estimate possible causes of fluid flow in the LHDAC, rates of flow, and the effects of flow on heat transport and temperature distributions.[19,21,28] Assuming that flow is convective, and driven by the temperature gradients across fluid regions, which produce buoyancy, several estimates regarding flow properties can be made through dimensional analysis.[46]

In free (also called natural) convection, the Grashof number Gr establishes the relative importance of buoyant, viscous, and inertial forces. It is defined as

$$Gr = \frac{g\rho^2 \beta \Delta T D^3}{\mu^2},$$ (1)

where g is the acceleration of gravity, ΔT is the temperature difference across the characteristic length scale of the fluid D, and ρ, β and μ are the material density, volumetric thermal expansivity, and dynamic (also called shear) viscosity, respectively. On the microscopic scale of the LHDAC the D^3 factor dominates, such that $Gr << 1$ is a good approximation. This implies that inertial forces are small compared to viscous forces, which balance the buoyant forces, giving a characteristic flow velocity U of[21,46]

$$U \approx \frac{\rho g \beta \Delta T D^2}{\mu}.$$ (2)

This is equivalent to stating that the ratio of inertial force to viscous force, or Reynolds

number Re, given by

$$Re = \frac{U\rho D}{\mu},\qquad(3)$$

is equal to Gr,

$$Gr \approx Re.\qquad(4)$$

Assuming liquid properties similar to water, a typical liquid dimension $D \approx 1\,\mu m$, and a temperature gradient of $\sim 10^3\,\mathrm{K\,\mu m^{-1}}$, then $Gr \approx 10^{-6}$ and $U \approx 1\,\mu m\,s^{-1}$. Speeds within several orders of magnitude of this value are expected for a realistic range of material properties and sample geometries. Such speeds would be consistent with detectable convective motion seen under microscopy in real time in experiments. However, this estimate is crude in that it does not account for the specific geometry of the LHDAC, the flow planform and position-dependence of velocity, the detected component of velocity, and other specific aspects of experimental systems. It has been reported[37] that the character and vigor of convection in the LHDAC sample chamber is noticeably sensitive to "the sample itself, the pressure medium, pressure, temperature, pressure-temperature gradients, and chamber geometry", and so is dependent on a complex interplay of sample properties, which are accounted for in this study.

When considering the character of convection and its influence on heat transport, we can also define the Rayleigh number Ra,

$$Ra = \frac{\rho g \beta \Delta T D^3}{\kappa \mu},\qquad(5)$$

which may be obtained by multiplying Gr and the Prandtl number $Pr = \mu/\rho\kappa$ (the ratio of viscous diffusivity μ/ρ to thermal diffusivity κ). At $Gr << 1$, Ra is also equivalent to the ratio of convective heat transfer to conductive heat transfer.[46] For the representative parameters of the LHDAC discussed above, $Ra \approx 10^{-6}$, and for any realistic set of parameters in the LHDAC $Ra << 10^3$, roughly the critical value of Ra in ideal systems below which convection is inhibited.[19,21] These considerations have been argued to lead to absent[19] or sluggish[21] buoyancy convection and a correspondingly negligible effect of convection on heat transfer in the LHDAC.[19,21,28] A complete quantitative consideration of these dynamics is explored in this study.

Numerical models have been used extensively to describe phenomena relevant to the laser-heated diamond cell, including temperature distributions[12,18,20–31,47] and, to a limited

5

extent, melting,[12,27,28] however fluid flow has not been directly modelled. In this paper, we present numerical finite-element models of natural thermal convection in the LHDAC, having a two-dimensional (axisymmetric) spatial geometry and axial orientation of gravity. We use time-dependent finite-element algorithms solving for thermal transport in the LHDAC (e.g. Montoya and Goncharov[27]), and include a Boussinesq fluid medium governed by the Navier-Stokes equations. Temperature gradients, sample physical properties, the occurrence of melt-solid boundaries inside heated samples, and the detailed configuration of typical sample chambers are accounted for by these numerical models of flow. Simulated samples, containing a solid metallic coupler on which laser energy is deposited, are fully fluid or locally melted by laser heating, with the melt boundary and location of melt determined self-consistently with the temperature gradient. Flow speed is found to be strongly controlled by fluid viscosity and by the particular geometry of the LHDAC. Maximum simulated flow velocities are at most small (of the order of tenths of $\mathrm{\mu m\,s^{-1}}$ for water-like viscosity), though are sufficiently fast to be observed in the laboratory. Natural thermal convection is thus confirmed to be possible in the LHDAC, though order of magnitude estimates of flow behavior discussed above have limited utility, revealing a need for detailed experimental models. The analysis of natural convection in the LHDAC developed here provides a reference model for flow and the forces that drive it, from which we consider possible alternative causes for flow and other types of motion that may occur in experiments. Ultimately, these models allow for a quantitative evaluation of experimental observations. Results are discussed in the context of motion observations previously made in LHDAC experiments and those that could potentially be made, such as velocity mapping of molten samples.

The simulation parameters and the equations of motion and energy are found in Section II. The model results in the steady-state limit are presented in Section III. Section IV discusses the physical and practical implications of the models and their relationship with prior work. A summary of conclusions drawn from our simulations and a discussion about future investigations is included in Section V.

II.   METHODOLOGY

A.   GEOMETRY

A DAC consists of two gem-cut diamonds pressed together at their culets, flat tips having a radius R_d on the order of tens to hundreds of µm. There is a gasket, a foil that is placed between the culets of the diamonds where a hole (of radius $R_m < R_d$) is cut. This gasket holds the sample inside the hole and between the two diamonds. To study transparent samples in the LHDAC, such as water, a thin metallic (or other optically absorptive) foil, known as the coupler (of radius $R_c < R_m$), is often introduced into the sample cavity to absorb laser radiation. To study opaque samples, such as Fe, a transparent pressure medium is placed around a foil in essentially the same configuration, with the medium acting as an insulator. The coupler may be held in place away from the diamond with grains of ruby or other material placed between the culet and the coupler. Melting of the medium or the coupler may be studied.[10] Optical access to the sample chamber is provided through the anvils.

The system modeled in this study represents this typical set up of a LHDAC experiment (Fig. 1). The modeled domain comprises a metallic coupler disk and a surrounding optically transparent pressure medium. The coupler is placed in the center of the cavity, and the medium is contained by the diamonds (on top and bottom) and gasket (laterally). The acceleration of gravity is set parallel to the DAC axis, which runs through the center of the culets, cavity and coupler. Assuming this geometry and laminar flow, the problem to solve is axisymmetric, i.e. there are no forces that would change the motion with respect to the angle ϕ, measured on the surface perpendicular to the axis. This common experimental geometry is convenient for numerical models and minimizes calculation time. Once this symmetry is assumed, the nominally 3D problem of flow becomes a 2D problem where there are variations only in r, distance to the axis, and z, position in the axial direction, as a function of time. The case of a horizontal axis (perpendicular to gravity), another common experimental configuration, must be modeled using all three spatial dimensions, presenting a more challenging problem not addressed here.

The coupler is heated on surfaces s_1 and s_2 by axially-aligned laser beams incident from top and bottom, and having equal power. This is a typical 'double-sided' laser heating
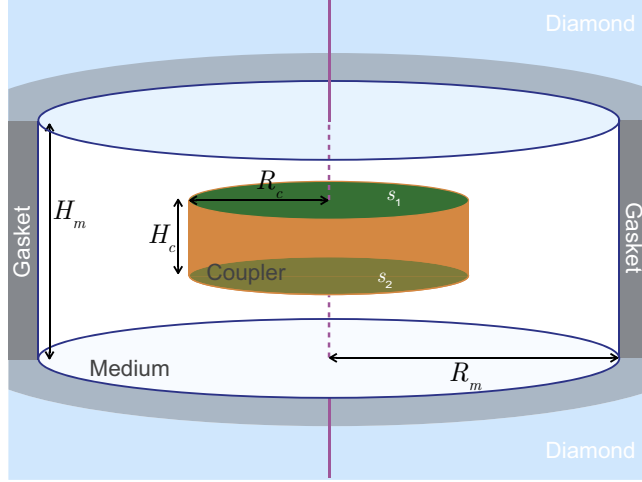
7

FIG. 1. This figure shows the schematic configuration of the modelled domain. We assumed a cylindrical symmetry around the axis shown in purple. The coupler disk (orange) is made of an optically opaque material and is heated with lasers on surfaces s_1 and s_2, shown in green. Inside the sample cylinder (white) the pressure medium is optically transparent and it is heated only by the heat transferred from the interior disk. Outer boundaries of the sample chamber are kept at a constant temperature of $300\,\mathrm{K}$.

configuration. We used the dimensions of a typical DAC, and of lasers currently used in LHDAC systems (see Table I). We assumed an ambient temperature ($T_{min} = 300\,\mathrm{K}$) boundary condition at the edges of the sample chamber, a good approximation for the LHDAC.[18,20,25,27,28,30]

TABLE I. Geometrical parameters used in the models. The LHDAC sample cavity is a cylinder of radius R_m and height H_m. The coupler is located at the center of the space and defined as a cylinder of radius R_c and height H_c, a distance $d = (H_m - H_c)/2$ from the diamond culets. The laser heating spots on the coupler have a radius parameter ℓ.

R_m (µm)	H_m (µm)	R_c (µm)	H_c (µm)	d (µm)	ℓ (µm)
50	16	30	4	6	15

In our models we treat melting of the transparent pressure medium and assume that the coupler remains solid. This is the configuration used to study dielectrics melting, as applied in many of the more reliable studies using motion-based melting curve determination

[195] ($MgSiO_3$[32,42,45] and NaCl[14,33] were mentioned earlier). The coupler is presumed to remain
[196] fixed in place, even when the surrounding medium is entirely fluid. For simplicity, we neglect
[197] any other material in the DAC other than the coupler and the medium.

B. PHYSICAL PROPERTIES OF MATERIALS

[199] Material properties used in the simulations are representative of materials commonly
[200] studied in the laser-heated diamond anvil cell (Table II). The medium was selected to have

TABLE II. Physical properties of the materials used in the simulations: mass density (ρ), heat capacity at constant pressure (C_p), thermal conductivity (k), thermal diffusivity ($\kappa = k/\rho C_p$), emissivity of the coupler (ϵ) and volumetric thermal expansion coefficient for the liquid phase (β). Values of medium viscosity (μ) and melting temperature (T_{melt}), were varied systematically for different simulations.

	ρ $\mathrm{kg\,m^{-3}}$	C_p $\mathrm{J/(kgK)}$	k $\mathrm{W/(mK)}$	κ $\mathrm{m^2\,s^{-1}}$	ϵ	β $\mathrm{K^{-1}}$
Coupler						
	9100	519	20	4.2×10^{-6}	0.272	$\ldots$[a]
Medium						
	1000	2000	10	2.6×10^{-6}	$\ldots$[a]	2×10^{-4}

[a] Quantity not defined

[203] physical properties similar to those of water in the range of 0-15 GPa, for fluid density
[204] ρ, heat capacity C_p, thermal conductivity k, and volumetric thermal expansivity β. In
[205] order to do a parametric study, we systematically varied selected properties of the medium
[206] which were found to have a first-order effect on flow behavior in the simulations, specifically
[207] the melting temperature (T_{melt}), which controls melt volume, and the melt viscosity (μ).
[208] Melt viscosities $\mu = 10^{-5}$, 10^{-3}, 0.1, 10, and 10^3 Pa s were tested. This range of values
[209] covers very low viscosity fluids such as liquid hydrogen ($\sim10^{-5}$ Pa s), water ($\sim10^{-3}$ Pa s),
[210] and silicate melts ($\sim10^3$ Pa s). Medium melting temperatures $T_{melt} = 300$, 400, 1000, and
[211] 2000 K were tested in primary simulations ($T_{melt} = 350$ and 1500 K were also tested in
[212] earlier simulations, partial results of which are presented here). We assume that physical

9

properties of the medium in liquid and solid states are identical, and that the medium is always optically transparent. The coupler is assumed to have properties similar to metals used in such experiments, specifically iron.

C.   GENERAL SIMULATION METHODOLOGY

In order to describe the dynamical behavior inside the DAC under various heating conditions we used a finite-element solution of the time-dependent energy transfer equation

$$\frac{\partial T}{\partial t} = -\mathbf{u} \cdot \nabla T + \kappa \nabla^2 T, \tag{6}$$

where T is the temperature, t is the time, and $\mathbf{u}$ is the flow velocity (with corresponding speed $v = |\mathbf{u}|$). For the solid, there is no flow and $\mathbf{u} = 0$. For the liquid region it is necessary to solve simultaneously the full Navier-Stokes equations

$$\frac{\partial \mathbf{u}}{\partial t} + (\mathbf{u} \cdot \nabla)\mathbf{u} = -\frac{\nabla P}{\rho} + \frac{\mu}{\rho}\nabla^2 \mathbf{u} + g\beta T\hat{\mathbf{z}}, \tag{7}$$

where P is the pressure and $g\hat{\mathbf{z}}$ is the downward acceleration of gravity. We used the solution for a Boussinesq fluid, where the changes in density are small and proportional to T, so the continuity equation reads as:

$$\nabla \cdot \mathbf{u} = 0. \tag{8}$$

Densities are assumed to remain constant throughout simulations and upon solid-liquid phase change; for the solid this means that thermal expansion effects are neglected; for the fluid, this means that thermal expansion is accounted for only through the Boussinesq approximation.

The heating lasers are assumed to have a Gaussian spatial intensity distribution $\mathcal{I}(r,t)$ at the coupler surface of

$$\mathcal{I}(r,t) = \frac{\epsilon \mathcal{P}(t)}{\pi \ell^2} \exp\left(-\frac{r^2}{\ell^2}\right), \tag{9}$$

where $\mathcal{P}(t)$ is the power of the laser, ℓ defines the radius of the laser spot, and ϵ is the surface emissivity. The heating is modeled to be continuous in time (i.e., $\mathcal{P}(t) = \mathcal{P}_o$), by raising the power in the first few 10^{-8} s of the simulation.

The simulations are initialized with all the cavity at ambient temperature (300 K), and flow velocities $\mathbf{u} = 0$. At $t = 0$ the laser is turned on, and the model develops the heat transfer and fluid motion out of equilibrium while heating the surfaces s_1 and s_2 of the

10

coupler. In each simulation, the temperature and velocity distribution are allowed to evolve to a steady state.

The temperature distribution in the sample is found to be identical whether or not flow terms are included in the simulations, confirming that heat advection does not contribute significantly to the heat transport in the case of natural convection, as expected from dimensional analysis. This fact allows for several simplifications in the models. Most importantly, the position of the solid-melt boundary is defined only by heat conduction, and so can be assessed *a priori* in simulations without the need to define it self-consistently with the flow, a significantly more challenging problem. Also, for all simulations at given $\mathcal{P}_o$, the maximum temperature T_{max} is effectively constant. Radiative contributions to heat transport are also negligible compared to the conductive contributions.[28,30]

The simulations were performed as follows. First, at a given $\mathcal{P}_o$, a simulation was run with two model domains (coupler and medium) assuming the medium was fully liquid ($T_{melt} = T_{min} = 300\,\mathrm{K}$) with water-like viscosity $\mu_w = 10^{-3}\,\mathrm{Pa\,s}$. This established a reference temperature distribution at this laser power. Next, a sequence of simulations at various values of μ and T_{melt} were performed. The solid-liquid boundary was identified by the isothermal contour in the reference temperature distribution corresponding to the melting temperature T_{melt}, which was used to divide the medium into solid and liquid domains producing a new geometry of three domains (coupler, solid medium, and liquid medium), as is appropriate for congruent melting.[28] To check the validity of this approach, the new location of the T_{melt} isotherm in the final simulation was compared with that in the reference simulation ($T_{melt} = 300\,\mathrm{K}$, μ_w), and the difference in isotherm position was found to be negligible. The sequential approach followed is thus physical for describing partial melting in the steady state limit.

The steady state was evaluated by observing flow velocity approach an asymptotic limit (Fig. 2). The time needed to reach steady-state equilibrium in the simulations is in the range of $10\,\mathrm{\mu s}$ to $5\,\mathrm{ms}$. It is longest for the lowest viscosities, because the viscous diffusion time, τ_μ, given as

$$\tau_\mu \approx \rho D^2 / \mu, \tag{10}$$

is larger for lower viscosity, approaching $\sim 3.6\,\mathrm{ms}$ for $\mu = 10^{-5}\,\mathrm{Pa\,s}$. For all other viscosities, viscous diffusion times are very rapid, and the equilibration is mainly controlled by the
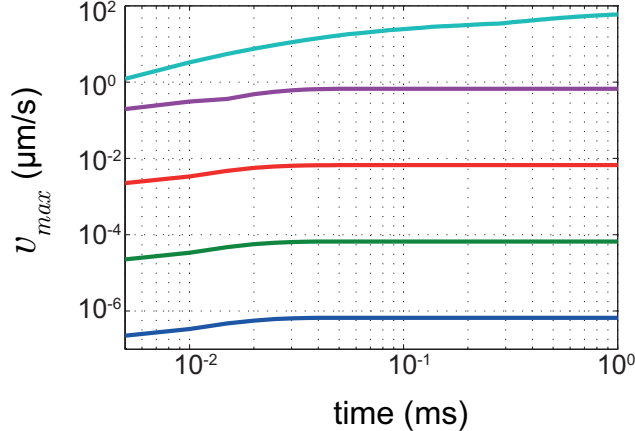
11

FIG. 2. Maximum velocity versus time for $T_{melt} = 300\,\mathrm{K}$, $T_{max} = 5051\,\mathrm{K}$ and $\mu = 10^3$, 10^1, 10^{-1}, 10^{-3}, and $10^{-5}\,\mathrm{Pa\,s}$ for blue, green, red, purple and cyan color lines, respectively. For the lowest viscosity, equilibrium is not achieved on the timescale of this plot. In the case of higher viscosities (bottom curves), the steady state is reached after $\tau_\kappa \approx 13\,\mathrm{\mu s}$; for low viscosity (top curve) steady state is not reached until $\tau_\mu \approx 4\,\mathrm{ms}$.

thermal diffusion time τ_κ, given as

$$\tau_\kappa \approx D^2/\kappa, \tag{11}$$

which is ~$13\,\mathrm{\mu s}$. Thus the approach to steady state equilibrium in the simulations is controlled by the longer of τ_μ and τ_κ.

In most simulations reported here, we defined the solid-melt boundary in the medium by a direct interpolation of the isothermal contour in the temperature distribution. In an earlier set of simulations, we used a simplified definition of the melt boundary defined by an ellipsoidal function, which approximated the shape and position of the solid-melt interface. This analytical boundary allowed for a faster numerical convergence, but generally showed more significant errors in defining the melt vesicle. Nonetheless, these results were found to be in good agreement with later, more accurate simulations in terms of scaling behavior (Section III B), indicating that the details of the shape of the melt package are not very significant for estimating the steady-state flow behavior.

12

D. LATENT HEAT EFFECTS

When the laser is turned on, the system heats up reaching a maximum temperature at the center of the coupler's surface T_{max} ($r = 0$ and $z = \pm 2\,\mu\text{m}$). When $T_{max} > T_{melt} > T_{min}$, a phase boundary must be created in the medium. Phase change generally requires the inclusion of a latent heat term in the thermal balance. We included the latent heat using the apparent heat capacity method (AHCM),[48] assuming a smooth transition from one phase to the other (and the presence of a mushy region), with g_l and g_s specifying the liquid and solid volume fractions, respectively. Considering heat conduction only ($\mathbf{u} = 0$), the numerical algorithm solves

$$\frac{\partial H}{\partial t} = \nabla \cdot (k_a \nabla T), \tag{12}$$

where H is the enthalpy, and the apparent thermal conductivity $k_a = g_s k_s + g_l k_l$, where k_s and k_l are the thermal conductivities of the solid and liquid phases respectively. This method uses an apparent heat capacity

$$c_a = \frac{dH}{dT}, \tag{13}$$

where

$$H = g_s \int_{T_{ref}}^{T} \rho_s C_s d\theta \; + g_l \int_{T_{ref}}^{T} \rho_l C_l d\theta + \rho_l g_l L, \tag{14}$$

such that L is the latent heat and T_{ref} is an arbitrary reference temperature; C_s, ρ_s and C_l, ρ_l are the heat capacities (at constant pressure) and densities from the solid and liquid phases, respectively. The apparent heat capacity (per unit volume) is then written as

$$c_a = g_s \rho_s C_s + g_l \rho_l C_l + \left(\int_{T_{ref}}^{T} (\rho_l C_l - \rho_s C_s)\, d\theta + \rho_l L \right) \frac{dg_l}{dT} \tag{15}$$

The numerical implementation thus solves the equation

$$c_a \frac{\partial T}{\partial t} = \nabla \cdot (k_a \nabla T). \tag{16}$$

In order to assess the effect of the latent heat, we again used the parameters in Table II for both liquid and solid phases, resulting in $c_a = \rho(C_p + L\, dg_l/dT)$ and $k_a = k$, such that outside the transition $c_a = \rho C_p$ [i.e. Eq. (16) is equivalent to Eq. (6)] and during the transition $c_a = \rho C_p + \rho L/\Delta T$. The melt fraction $g_l = 1 - g_s$ is assumed to increase with T from 0 to 1 at T_{melt} over an interval of $\Delta T = 1\,\text{K}$. This step-like function approximates congruent melting.[28]

13

In this case, the only signatures of the phase change in the simulation will be those directly due to the latent heat. Choosing a value for the latent heat to be $L = 300 \, \text{kJ/kg}$ (similar to water ice melting) we solved the finite element model and compared it to the solution with $L = 0$ (Fig. 3). We observe that when latent heat was accounted for the maximum
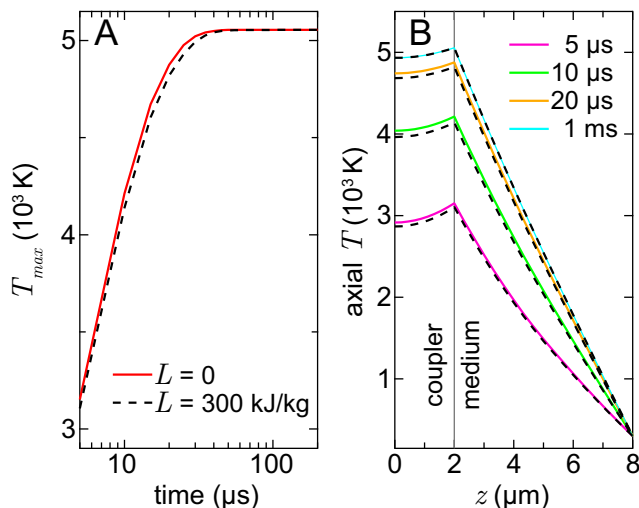

FIG. 3. Effect of latent heat of melting. Models with latent heat $L = 0$ and $L = 300 \, \text{kJ/kg}$ are compared, for maximum laser power, $T_{melt} = 400$ K, and neglecting fluid flow. A, time series of the temperature at the center of the coupler surface. The temperature grows faster for $L = 0$ (solid line) than for $L > 0$ (dashed line), but reaches the same equilibrium value. B, temperature profiles through the axis of the DAC from the center to the culet for four different snapshots at $t = 5$, 10, 20, and 1000 µs, for $L = 0$ (solid lines) and $L = 300 \, \text{kJ/kg}$ (nearby dashed lines).

temperature is reached later than in the case of $L = 0$. However, both simulations reach identical maximum temperatures in the steady state limit. It is also possible to observe that the temperature distribution over the DAC axis (Fig. 3B) depends on latent heat at earlier times but is identical later in the simulation. This can be expected since $\partial T / \partial t$ vanishes when the steady state is reached, and the solution of Eq. (16) becomes independent of L. Thus latent heat has no effect on temperatures for steady-state conditions.

14

III. RESULTS

A. GENERAL OBSERVATIONS

All models develop temperature profiles that are symmetric about a horizontal plane through the center of the sample, due to use of double-sided laser illumination (Fig. 4A), with T_{max} reached at the axial point on the illuminated surfaces. For all models T_{min} is constant but the change in laser power changes T_{max} and the isothermal contours, and thus melt vesicle shape and size for a given T_{melt}. The solid:liquid volume ratio in the medium ranged from zero (fully molten medium, $T_{melt} = 300\,\mathrm{K}$) to 0.995 (having two small melt vesicles at the laser-heated spots).

The steady state flow we find for the simulations has a constant general geometry. For the fully fluid runs ($T_{melt} = 300\,\mathrm{K}$) three convection cells develop, with one forming away from the coupler at the sample edge (Fig. 4B); maximum velocities are found next to the coupler's outside edge (Fig. 5) and have an upward axial direction. Where the pressure medium is partially melted ($T_{melt} > 300\,\mathrm{K}$), there are two main convection cells where maximum velocities are directed radially inward (outward) for the sample above (below) the coupler (Fig. 4C-E). Maximum flow velocity is located in a ring $\sim 1\,\mathrm{\mu m}$ above and below the coupler with a radius of several $\mathrm{\mu m}$ (Fig. 5).

The flow and the maximum velocity are given by pressure imbalances due to the strong thermal gradients and resulting buoyant forces. There is a correlation between maximum velocity and differential pressure across the fluid, as well as melt geometry (Fig. 6). Both maximum velocity and maximum pressure difference are larger for larger values of T_{max} and lower values of T_{melt}. Models with a fully fluid medium (lower part of Fig. 6A) and a convection pattern with a dominant cell away from the coupler (Fig. 4B) show larger velocities (by a factor of ~ 2) than models with partial melting and fluids confined close to the coupler (upper part of Fig. 6A). This is due to a shift in the planform of convection rather than to a change in driving pressure, which scales gradually with T_{max} and T_{melt} (Fig. 6B). The maximum pressure difference across the fluid region is $0.036\,\mathrm{Pa}$, for the largest T_{max} and lowest T_{melt}, i.e. for fully liquid medium and highest peak temperature. That is, the larger the fluid volume and temperature variance, the larger the pressure difference across the volume resulting in faster flow speeds (Fig. 7).
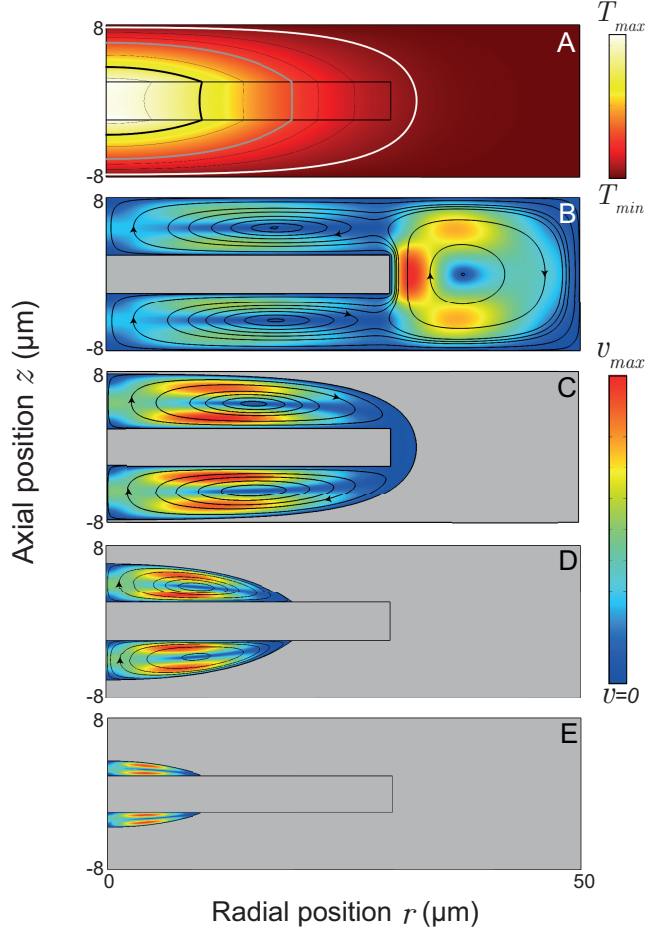
15

FIG. 4. Axisymmetric cuts of temperature and velocity magnitude for $T_{max} = 2675\,\text{K}$. A, temperature map; color indicates temperature; white, grey, and black lines are isothermal contours for 400, 1000, and $2000\,\text{K}$, respectively. B, C, D, and E, velocity maps for $T_{melt} = 300$, 400, 1000, and $2000\,\text{K}$, respectively; color indicates speed, with $v_{max} = 0.337$, 0.159, 0.0518, and $1.93 \times 10^{-3}\,\text{µm s}^{-1}$, respectively, for μ_w $(10^{-3}\,\text{Pa s})$; black lines show the flow streamlines with arrows indicating the direction of the flow.

B.   SCALING BEHAVIOR

The velocities found at a given T_{melt} and T_{max} (i.e. for a given melt geometry) scale in direct proportion to viscosity (Fig. 8). Setting a reference value for viscosity to be $\mu_w = 10^{-3}\,\text{Pa s}$, if a corresponding velocity is v_w, we find that for simulations differing only in the assumed value of viscosity the velocity generally scales as $v = (\mu_w/\mu)v_w$. Model results for velocity presented here at this reference viscosity (i.e., Figs. 4 to 7 and 10B) can be
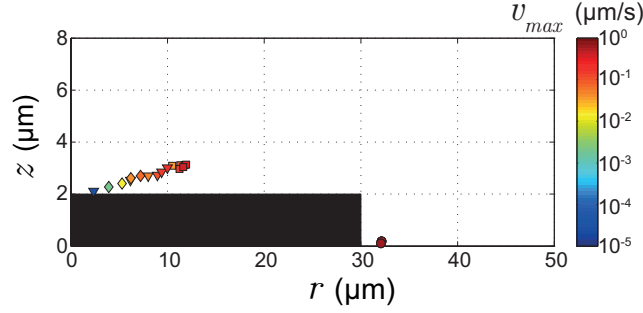
16

FIG. 5. Location of maximum velocity in the upper half of the sample (bottom half is symmetric). Colors indicate the velocity magnitude for μ_w. The symbols represent $T_{melt} = 300, 400, 1000$, and 2000 K for $\circ$, $\square$, $\triangledown$, and $\diamond$, respectively. At maxima locations above the coupler, flow is radially directed; for maxima outside the coupler ($T_{melt} = 300$ K) flow is axially directed.
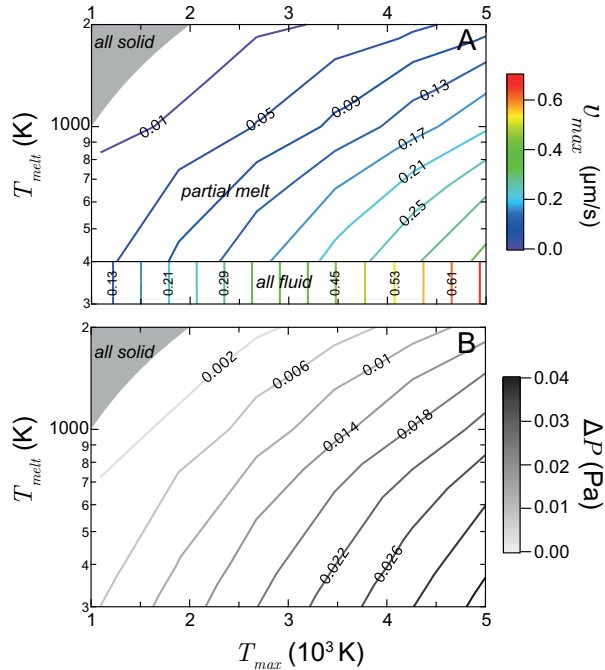

FIG. 6. Contours of A, maximum flow velocity (v_{max}) and B, maximum pressure difference across the fluid (ΔP) as a function of T_{melt} and T_{max}, for μ_w. Velocities at other viscosities can be accurately obtained by multiplying values in A by the ratio of μ_w/μ, whereas ΔP is identical for all μ. A is separated into two zones depending on the location of the velocity maxima: vertical lines at $T_{melt} = 300 - 400$ K correspond to a fully fluid case ($T_{melt} = 300$ K) and contours at $T_{melt} = 400 - 2000$ K are for partial melting ($T_{melt} \geq 400$ K).
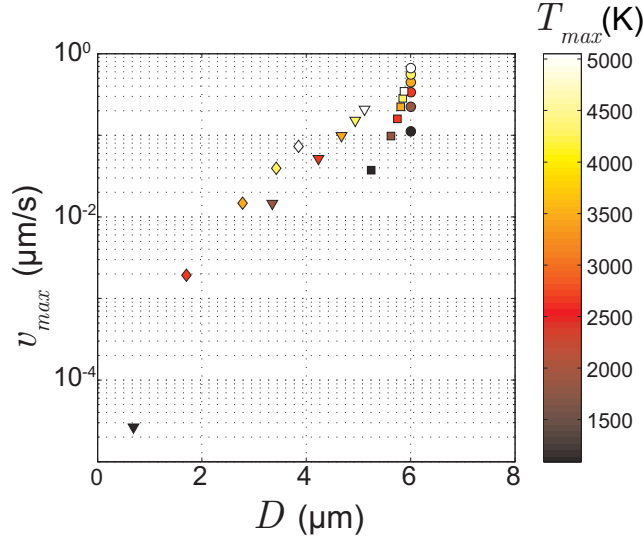
17

FIG. 7. Plot of maximum velocity versus the characteristic flow length-scale (D) for μ_w. The symbols correspond to simulations with $T_{melt} = 300$, 400, 1000, and 2000 K for $\circ$, $\square$, $\triangledown$, and $\Diamond$, respectively. The colors correspond to T_{max} in the color bar.

364 accurately adjusted to describe other viscosities using this scaling relationship.
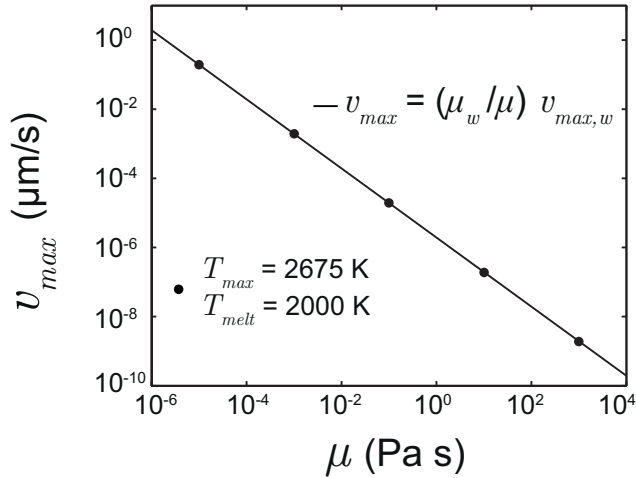

FIG. 8. Scaling of peak velocity v_{max} with viscosity μ for a series of simulations at fixed melt volume as shown in Fig. 4E ($T_{max} = 2675$ K, $T_{melt} = 2000$ K).

365 Following Section I we expect that for the present experimental system $Re \simeq Gr$ should
366 provide a good approximation for the dynamics. Indeed, one of the key predictions of this
367 model is the inverse proportionality of v_{max} and μ [Eq. (2)], as seen in the simulations
368 (Fig. 8). We therefore calculated Re and Gr for our dataset to compare with the predictions

18

of dimensional analysis. Given the geometry of this system (Fig. 9A) and our approximation that the thermal conductivity of the medium is constant and identical in solid and liquid, the axial temperature gradient in the medium is linear (Fig. 9B), and we may transform Re and Gr into known (measurable) parameters in our experimental setup: the maximum temperature, T_{max}, located on the axis of symmetry; the melting temperature T_{melt}; the minimum temperature T_{min} corresponding to the anvil surface; and the thicknesses of the medium d and the melt D along the axis. Hence D is the characteristic length scale of the fluid vesicle. The temperature difference across the liquid zone is then
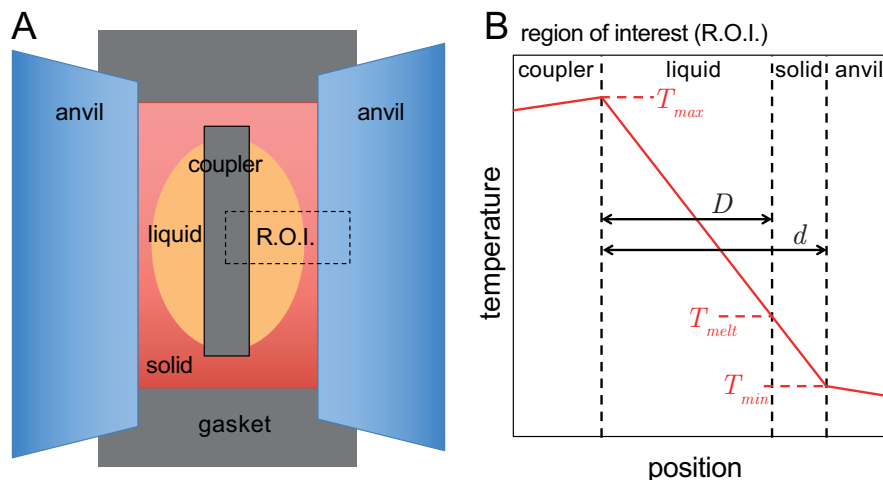

FIG. 9. Simplified geometry of a laser-heated diamond cell. A, the LHDAC configuration. B, a 1D view along the axis of symmetry. Panel A highlights the region of interest (R.O.I) around the axis of symmetry corresponding to the temperature distribution in B.

$$\Delta T = T_{max} - T_{melt} \qquad (17)$$

and

$$D = \frac{T_{max} - T_{melt}}{T_{max} - T_{min}} d \qquad (18)$$

With these definitions, we plotted Re versus Gr, assuming $U = v_{max}$ (Fig. 10).

The dynamic behavior thus obtained follows a relationship $Re \propto Gr$, previously suggested by the dimensional analysis [Eqs. (2) and (4)], but Re and v_{max} for any given Gr are lower than expected by roughly three orders of magnitude. We can represent the results, for any given set of conditions, using a proportionality factor A, i.e.
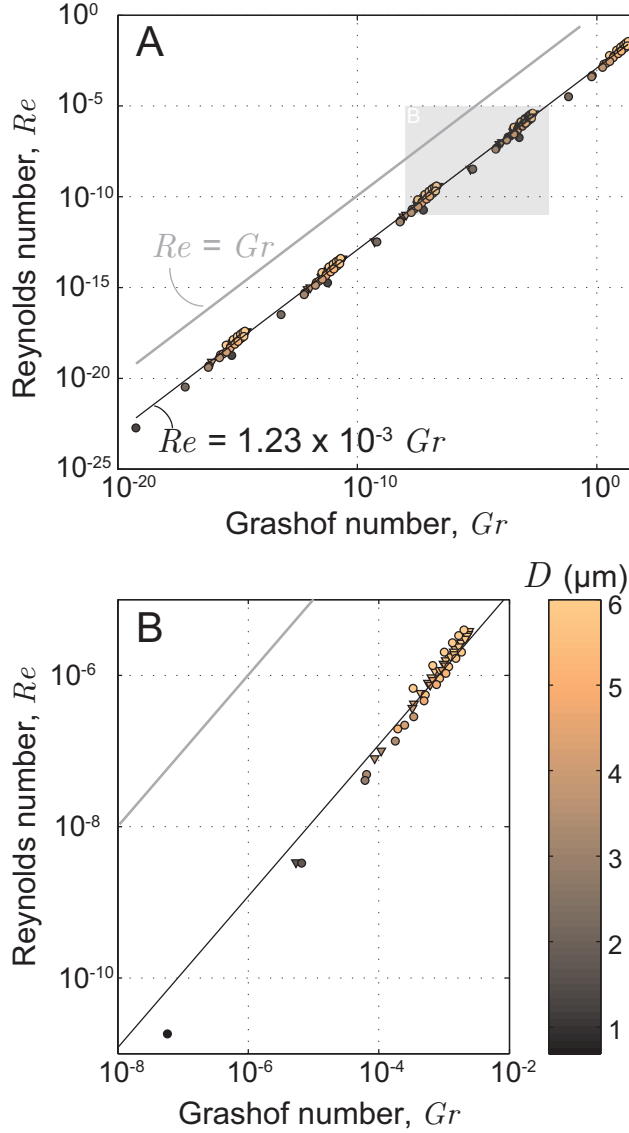
$$Re = A\,Gr, \qquad (19)$$

19

FIG. 10. Reynolds number Re versus Grashof number Gr for the complete set of model results. The colors and color bar correspond to the characteristic length scale (D) for each simulation. The solid black line is the fit to the relation $Re = A\,Gr$ [Eq. (19)], taking A as a constant. The grey line is the upper bound[21] on Re [Eq. (4)]. The circles represent simulations that used the isothermal contour at T_{melt} to define the solid/liquid boundary while the triangles are simulations that used an ellipsoidal function to estimate the boundary position. Panel A shows all simulation results; the fit of Eq. (19) to these data gave $A = 1.23 \times 10^{-3}$. Panel B shows only results from simulations with μ_w, from the grey region of A.

where A is found to be approximately constant, with the total set of simulations obtained closely described with a value of $A = 1.23 \times 10^{-3}$. This is consistent with the expectation that Eq. (2) provides an upper bound ($A \leq 1$) for velocity in the system.[21]

The value of A is insensitive to the specific geometry and size of the fluid region: it is nearly the same for complete melting (Fig. 4B) as for local melting confined to near the laser hotspot (Fig. 4E). Some higher-order deviations from a fixed A are evident, such as weakly decreasing A with melt volume (Fig. 10B). In general, different geometries for specific experimental set ups yield different values of A, sensitive to relative axial and radial dimensions, laser spot size, the orientation of gravity, and other assumed characteristics of the system.

While the prior analysis followed from the assumption that $Gr << 1$ and hence $Re \propto Gr$ for the LHDAC, we find $Gr \gtrsim 1$ at the upper limit of the simulated range (Fig. 10A). At such conditions, dimensional analysis implies the inertial contribution to the force balance should become non-negligible, manifesting as a different scaling law[46] similar to $Re \propto \sqrt{Gr}$. However, in our simulations there is no evidence for a deviation from the linear relationship. This is likely due to the inertia being smaller than expected from dimensional arguments. The scaling laws obtained here thus remain approximately valid throughout the realistic parameter space of the LHDAC.

Combining Eqs. (17) to (19), the maximum fluid velocity in the liquid medium can be described by

$$v_{max} = A\,\lambda \frac{d^2}{\mu} \frac{(T_{max} - T_{melt})^3}{(T_{max} - T_{min})^2}, \tag{20}$$

where

$$\lambda = \rho g \beta \tag{21}$$

is a constant from the physical properties of the material.

While coupler melting was not included in the simulations, coupler and medium melting share a number of similarities that allow some predictions regarding convective flow in the coupler. In the limit of small melt volume, melt vesicles in the coupler and medium have similar size and shape,[10] similar boundary conditions (i.e. $T_{melt} \leq T \leq T_{max}$), and are expected to exhibit similar flow planform given that flow is symmetric for vesicle inversion (Fig. 4D-E). With these similarities, the relationship $Re = AGr$ [Eq. (19)] should also hold

21

for coupler melting, with similar values of A, and may be expressed as

$$v_{max} = A\lambda\frac{D^2}{\mu}(T_{max} - T_{melt}).$$ (22)

Together with the earlier conclusion that flow systematics depend little on the particular geometry of liquid regions, we conclude that a simple scaling law, similar to Eq. (22), generally describes the thermal convective flow within melts in the LHDAC. Another scenario that likely follows these systematics is that of direct laser heating and melting of a semi-transparent medium.[6,21] However, cases where both medium and a coupler melt could be potentially more complicated: while the above law [Eq. (22)] would plausibly hold for minor interfacial deformations observed in such experiments that preserve the basic shape and size of the melted region,[44,49] larger distortions including hole and droplet formation and multiphase mixing,[50] and associated surface tensions (see Section IV), could significantly alter flow behavior.

IV. DISCUSSION

The well-defined relationship between viscosity and convective flow speeds in the LHDAC suggests velocimetry as a means to establish viscosity in convecting fluids under pressure. At fixed size of melt, velocities are inversely proportional to viscosity [Eq. (22) and Fig. 8], and so can vary by many orders of magnitude over the plausible range of viscosities encountered in fluids. Velocities also increase by orders of magnitude (at constant viscosity) with the size of the molten region (Fig. 7), which is controlled by initial sample dimensions, melting temperature, and peak temperature, and may be estimated from these known parameters [e.g. Eq. (18)] or through direct observation. Velocity is also linearly dependent on density and thermal expansivity, but given that these are well constrained and relatively invariant under pressure, their uncertainty should not play a major role in viscosity determination. Thus, viscosity and melt dimensions are the primary variables determining the convective flow behavior for any given sample configuration, with the latter being independently measurable. There are hence good prospects for measuring high-pressure viscosity if convection in the LHDAC can be observed and characterized.

It is evident that while thermal convective flow is possible in the LHDAC, it is more sluggish than previously predicted[21] and may be challenging to detect in many cases. For

22

viscosities on the order of mPa s (similar to water), fluid velocities in LHDAC samples due to buoyancy flow are expected to be $\lesssim 1\,\mu m\,s^{-1}$ (Fig. 7). Assuming a minimum detectable flow velocity of $0.01\,\mu m\,s^{-1}$ (or roughly $0.1\,\mu m$ per minute) it is evident that in some of the possible parameter space for the LHDAC convective flow will be detectable (Fig. 11). This limit assumes that material would have to move by a significant fraction of the wavelength of visible light (about 1 μm) on a typical experimental timescale (about 1 minute) to be detected optically, such as by direct visual observations[3,8,9,19,32,36,37] or by interference changes (i.e. the 'speckle method').[10,33–35,38–41] Thermal convection should thus be readily visible for
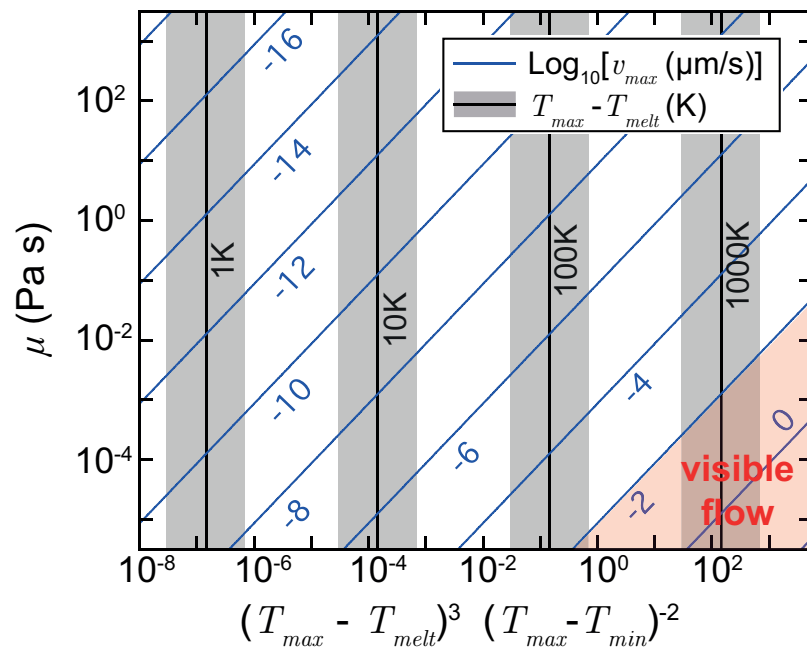

FIG. 11. Flow velocity as a function of viscosity and temperature above melting. Blue lines are velocity contours labeled with the logarithmic velocity in $\mu m\,s^{-1}$, after Eq. (20). Black vertical lines with grey envelopes are the conditions of experiments where peak temperature (1,500-6,000 K) exceeds the melting point by 1, 10, 100, and 1000 K. The red shaded region in the lower right represents the domain where natural convection could be readily observed ($v_{max} > 10^{-2}\,\mu m\,s^{-1}$).

viscosities similar to water, or lower.

Furthermore, the melting temperature must be exceeded significantly, by 100-1000 K according to our models (Fig. 11), before convection is detectable. Naturally, D and $T_{max} - T_{melt}$ (and hence convective vigor) [Eq. (22)] tend to zero as $T_{max} \to T_{melt}$, and convection at the melt temperature is not possible regardless of the size of the molten region;

but our results show that considerable overheating is necessary to produce observable flow. This questions the feasibility of reliably detecting melting via convective motion, suggesting that significant overestimates of melting temperature are possible if convective motion is used as a criterion. Indeed, in experiments, initial motion associated with melt may be difficult to see, with 'clear, continuous convection' observed only several hundred degrees K above the putative melting point.[36,37] However, it should be noted that measurements using *in-situ* motion-based criteria more often underestimate melting temperatures compared to other measurement techniques and theoretical predictions.[1,4,14–17,42–44] This suggests that the motion observed in many experiments at proposed melting points may not be due to thermal convection, but other causes, as considered in more detail below.

The significant overestimation of velocity using order of magnitude dimensional arguments[21,46] can be explained, in part, by the very confined geometry of melts in the LHDAC, such that the convecting material is at all points being deflected by the boundary of the liquid region rather than freely rising and falling in free space. That the factor A decreases with the size of the molten region (Fig. 10B) is further suggestive of this confinement effect.

Another apparent control on peak velocity is that the simulated geometry approaches that of plane-layer convection near the laser heating spot. In perfectly plane-layer (i.e. Rayleigh-Bénard) natural convection, with liquid confined in a horizontal layer, perpendicular to gravity, across which a temperature difference is imposed, convection is inhibited for sub-critical Ra (i.e. $Ra \lesssim 10^3$, as characterize the LHDAC). This stability criterion does not generally apply in the LHDAC due to the horizontal thermal gradients.[21] However, horizontal gradients tend to zero close to the sample hotspot (at $r = 0$, Figs. 4 and 9), and this evidently inhibits flow in this region. Despite this near-hotspot region having the largest local liquid thickness D and local temperature gradient $|\nabla T|$, peak velocities tend to occur elsewhere, in adjacent areas of the melt (Fig. 4C-E) having smaller D and $|\nabla T|$ (Fig. 4A) but nonzero horizontal temperature gradients $\partial T/\partial r$. This contrasts with expectations from the scaling behavior developed and validated generally in this work that flow velocity should follow a relation similar to

$$U \propto D^3 |\nabla T|. \tag{23}$$

Consequently the largest flow velocities in the LHDAC occur not at the hotspot, but rather around it in a toroidal or ring-like convecting region (see also Fig. 5). This further reflects the strong geometric controls on convective vigor in LHDAC melts.

24

Buoyant pressure differences across liquid regions that drive natural convection are exceedingly small (of order 10^{-2} Pa, Fig. 6B), and so if convective motion is possible, motions driven by other forces of larger magnitude are also possible and, when present, may supersede convection as the dominant mechanism of motion. Non-hydrostatic pressure gradients across solid samples imposed on compression in typical DAC experiments can be of the same order as the static pressure, i.e, $\sim 10^9$ Pa, and could drive sudden, rapid motion as melting occurred. Boundaries in samples (such as planar coupler-medium interfaces) also routinely deform near melting, often into a bead- or droplet-like features[3,9,32,35,36,44,49] presumably arising from surface tension; the pressure associated with surface tension is of order $2\gamma/R$ or $\sim 10^3$ Pa for equilibrium interfacial radius of curvature $R \approx 10^{-5}$ m (determined experimentally[44,49]) and typical surface energy $\gamma \approx 10^{-2}$ N m^{-1}. Also significant are stresses induced by thermal expansion upon heating to the melting point (of order $\beta K_T[T_{melt} - T_{min}]$ or $\sim 10^9$ Pa, for bulk modulus $K_T \approx 10^{10}$ Pa and $T_{melt} \approx 10^3$ K) or by phase transformation, i.e. induced by the melting process itself (of order $K_T \Delta V/V$ or $\sim 10^8$ Pa, for relative volume change $\Delta V/V \approx 1$ % as in high-pressure melting). In addition to the associated forces being significant in the context of driving fluid flow, phase change,[39,42] surface tensional adjustment, and thermal expansion imply motion directly. Brownian motion has also been proposed as a cause of motion in the LHDAC,[19] though this effect seems limited to cases where mixed phases are present, such as for inhomogeneous or incongruent melting, suspensions or colloids.

Most of these phenomena and the associated forces (with the exception of Brownian motion) would be transient in nature, annealing out with time at constant temperature, and so flow and other motion due to them might dissipate as an equilibrium state is reached, and be distinguishable from the continuous motion of thermal convection achieved in the the long-duration limit (the scenario examined in this study). Transient modes of motion reported in experiments,[36,37,39] such as 'occasional small movements', 'abrupt, discontinuous change', or 'disappearance' of motion, may possibly originate in temporary, annealing driving forces. In the interest of interpreting motion in terms of material viscosity, it is expected that the character of motion depends on and can indicate the primary driving mechanism; observations of flow planform, duration, and temperature-dependence could help isolate the appropriate physical model and thereby enable viscometry. Perhaps most usefully, we find that it is reasonable to interpret persistent motion as being due to convection as it seems difficult to explain this generally through other means.

25

Thermal instabilities that create thermal pressure fluctuations in an already molten sample have also been previously proposed as driving continuous flow,[19,28] however this possibility is difficult to substantiate. A thermal perturbation ΔT_i, operating through thermal expansion, could drive flow at a velocity comparable to natural convection if $\Delta T_i \approx \Delta P_i / \beta K_T$ where ΔP_i is the buoyant pressure difference across the fluid region in convection, i.e. $\sim 10^{-2}$ Pa (Fig. 6). This implies $\Delta T_i \approx 10^{-7}$ K. Such temperature fluctuations are almost certainly present even under the most stable heating conditions. However, thermal pressure fluctuations of this type relax very quickly in hydrostatic conditions, on the timescale of pressure wave propagation, $\tau_s \simeq D/v_B$, where v_B the bulk sound velocity – i.e within ~ 1 ns. This is probably not sufficient time to produce detectable flow even if the pressure perturbations, and the associated flow speeds, were substantially larger than for natural convection; moreover, as the thermal response time of the LHDAC is significantly longer than this ($\tau_\kappa >> \tau_s$) it seems unlikely that large-scale thermal pressure perturbations could be imposed within the required timescale. Thus we conclude that differential thermal pressures are probably not produced in the fluid in nominally continuous heating. A plausible way thermal fluctuations could influence flow would be via the buoyancy force itself. To further examine this issue of instability driven flow, we have tested flow sensitivity to temperature fluctuations in our simulations by introducing a sinusoidal instability in the laser power and examining its influence on flow (Fig. 12). For μ_w, only fluctuations at a frequency below ~ 100 kHz influence the flow significantly. This is due to the finite response time of the system (Section II C), on the order of microseconds (τ_κ) in this case, such that more rapid fluctuations in laser power are damped and only weakly influence temperature while having no discernible influence on flow. In cases where the flow is influenced, convective flow velocity is only weakly modulated, and thus this phenomenon is not likely to enhance detectability of motion beyond that of steady thermal convection. While thermal fluctuations are thus unlikely to directly lead to detection of fluid motion, they may indirectly lead to motion via the rapid conductive adjustment of temperature gradients producing, for example, phase changes and melt boundary migration.[39,42]

In any case, the alternative forcings explored above can in principle modify the fluid flow but do not affect the relationship between flow onset and melting. However, on a final note, solids in a high-temperature solid-solid phase transforming,[10,15,39,51] rapidly recrystallizing,[4,10,16,17,42,52] or thermally-softened[14,17,42,43] regime could also play a role in
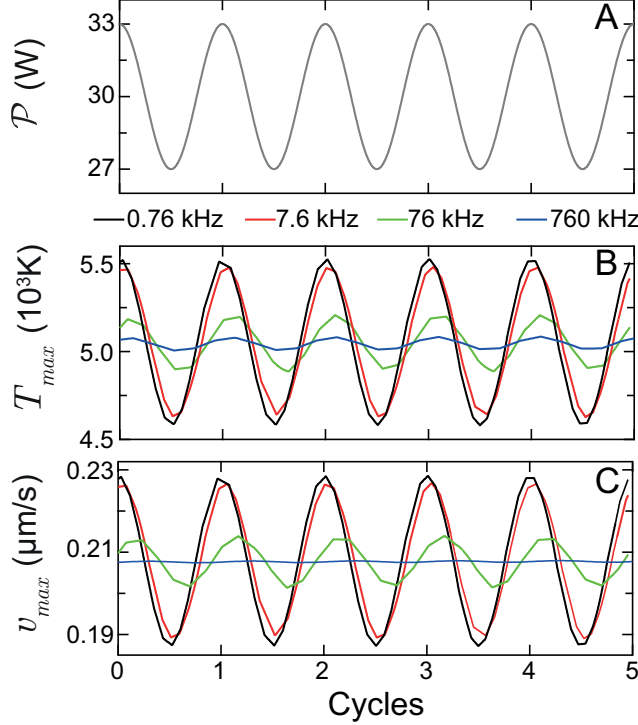
26

FIG. 12. Effect of fluctuating laser power (A) on temperature (B) and flow velocity (C) for frequencies ranging from 0.76 to 760 kHz, for μ_w, $T_{melt} = 1000\,\mathrm{K}$, and $T_{max} = 5051\,\mathrm{K}$. Above 100 kHz ($\sim 1/\tau_\kappa$), the effect of fluctuations on temperature is dramatically reduced and the effect on velocity is negligible and damped by the response time of the system. Variations in fluid dimensions due to temperature change were not considered.

559 thermally induced motions, and in some cases solid states might respond to the same forces
560 that could affect the fluid states – even, possibly, to the buoyant force. For example, in
561 principle a viscoelastic state[17] could undergo thermal convection; or recrystallization could
562 be induced by the buoyant stresses. Such phenomena could lead to underestimation of melt
563 temperature by motion criteria (cases of Fe[3,4] and Ta[16,35,44] have been discussed), however
564 the behavior of solids is beyond the scope of this study.

565   Accounting for latent heat associated with melting only influences the behavior of the
566 sample when temperatures are unsteady – for example, when temperatures are changing
567 as the simulation is heating up and approaching an equilibrium steady-state (Fig. 3). In
568 the steady-state limit, phase change is not occurring and no energy is used in transforming
569 material, so latent heat does not play a direct role in defining the temperature distribution
570 in the sample, the position of the melt boundary, or the laser power required to sustain the

given temperature. This is consistent with previous conclusions[27,28] that latent heat alone has little to no effect on the thermal response of the LHDAC, particularly in the steady state limit. Thus our result supports the conclusion that 'plateau'-like deviations from a smooth, continuous increase in temperature with laser power, often seen experimentally near melting and often associated with visible motion,[3,6,9,19,36,37,41,45] cannot be caused by latent heat and must instead be caused most directly by changes in material physical properties[27,28] or dynamic phenomena such as rapid convective heat transfer.[28] While our study rules out natural convection as a cause of the plateau effect, flow driven by other forces, as discussed above, might play a role if it were particularly vigorous and persistent.

V.   CONCLUSIONS

This study confirms that natural convection is possible in fluids in the laser-heated diamond anvil cell for a typical experimental configuration, consistent with previous order-of-magnitude estimates[21] and qualitative assessment of experiments.[3,9,32,34,36–42] Natural convective motion cannot affect the energy balance of the diamond cell – thermal conduction remains the dominant mechanism of energy transfer in the LHDAC – so the natural convection can be thought of as a passive response to temperature gradients. Flow velocities are found to be significantly less than the upper bound expected on the basis of dimensional analysis.[21,46] We found that the dynamics of natural convection in the LHDAC follow a scaling law [Eq. (22)] where the Reynolds number (Re) is proportional to the Grashof number (Gr), or $Re = AGr$, with a constant of proportionality $A \simeq 10^{-3}$. This scaling behavior is expected to be of general validity for the LHDAC when gravity is parallel to the symmetry axis.

The routine, wide-ranging observations of motion at high-temperatures in the LHDAC,[3,8–10,19,32–41] the observation of 'vigorous' and rapid motion, and the common attribution of this motion to melting and convection, is somewhat in contrast with our conclusion that convective fluid flow would be difficult or impossible to observe in real time when the melting point is just exceeded (Figs 6A and 11). Flow speed increases quadratically with the length scale of the molten region and linearly with the temperature difference across the melt [Eqs (2) and (22)], such that convective flow appears gradually above the melting point, strengthening with increasing peak temperature (and hence melt volume) and becoming

28

realistically detectable only when the melting point is significantly exceeded (by 100-1000 K in representative cases). Thus relating an observation of genuine convective motion to melting is not straightforward, and suggests most directly an upper bound on melt temperature. Documented motions with different behavior, such as a sudden onset of vigorous motion with increasing temperature, or transient motion at constant temperature, might be driven by other forces (related to sample annealing), and could occur at or nearer to precise melting points, and potentially below them (as for fast recrystallization[4,10,16,17,42,52]). Indeed, non-convective motions could dominate in a number of scenarios. There is thus a need to identify the dominant causes of flow and motion in the LHDAC and hence the relationship of these motions to melt temperatures and melt properties. Continuous, steady fluid motion is likely an indication that convection is occurring, providing a simple initial test of whether the observed process of motion is plausibly convective in nature. Our study predicts specific observables, such as convection in a ring or torus for axially oriented gravity, annealing-driven flow, and temperature-dependence of flow vigor, that can better inform the true nature of flow phenomena, and their origin in convection or otherwise.

Another common criterion for high-pressure melting are anomalies (such as plateaus) in temperature observed when increasing laser power through melting points.[3,6,9,19,36,37,41,45] Our models rule out both latent heat of melting and fluid flow as potential causes for these anomalies, assuming well-annealed samples at thermal equilibrium. This restricts the possible origin of such plateaus, with the most probable remaining general explanation being changes in material properties upon melting (e.g. thermal conductivity, heat capacity, or optical properties). Studies of motion and temperature as a function of both laser power and time since power increase could yield valuable information about the nature of motion, its principal causes, and its relationship to melting and other common melting criteria.

It is interesting to note that, as demonstrated in our simulations, pressure gradients can never be fully annealed in the LHDAC as buoyant pressure differences always exist. Whether the liquid (or solid) responds to these buoyancy forces on an experimental timescale is dependent on the material properties. Buoyant forces should become increasingly important at high temperatures where material softening, melting, recrystallization and other forms of annealing are increasingly available to relax shear stresses.

The measurement of fluid transport properties at conditions of extreme pressure and temperature is a longstanding challenge. Due to the strong control of flow speed by viscosity

in LHDAC convection, there are good prospects for determining viscosity at high pressure using the melt production and flow behavior induced by laser heating. If the origin of flow is natural convection, the flow velocity is inversely proportional to viscosity [Eq. (22)]. Since viscosity varies by roughly 10 orders of magnitude over the typical viscosity range of natural fluids, the relatively minor uncertainties in the other parameters appearing in the scaling model [Eq. (22)] (e.g. melt size, melt temperature, and peak temperature) do not have a major influence on determining, at least, the order of magnitude of viscosity. If melt dimensions could be assessed precisely, for example by direct observation as part of fluid velocity measurements, the quality of the viscometry could be particularly accurate. Recent efforts to quantify motion via the changing speckle pattern of laser light reflected from molten samples suggests one way to assess the vigor and rate of flow,[41] however a physical understanding of the relationship between speckle changes and flow rates must be established. In any case, more direct probes of flow rates, streamlines, and spatial distributions may be required to provide a complete comparison to models and suitable data for accurate viscometry.

Observation of convective motion alone can be enough to place a significant constraint on viscosity. Only convective flow in fluids with viscosities similar to water ($\sim 10^{-3}\,\mathrm{Pa\,s}$), or lower, are readily detectable in the LHDAC according to our simulations (Fig. 11). Meanwhile, condensed fluids rarely exhibit viscosities much lower than $10^{-4}\,\mathrm{Pa\,s}$ (group 1 and low-Z group 18 elements being notable exceptions). Thus it is likely that, in most cases, detectable convection corresponds to a viscosity within about an order of magnitude of that of water. For example, the routine observation of apparent convective motion in molten Fe under pressure[3,8,9,36] is consistent with the common assumption that molten Fe at Earth's core conditions has a viscosity similar to water.[2,53] This also suggests that melt detection by sample convective motion should not be possible for viscous melts such as silicate liquids.

In summary, the intrinsic natural convection in melts produced by laser heating in the diamond anvil cell may be one way of measuring fluid viscosities at extreme pressure and temperature. In addition to providing essential data on fluid transport under pressure, as relevant to melts in planetary deep interiors, high-pressure viscosity measurements offer one way to characterize pressure-induced changes in fluid bonding and structure that may be otherwise difficult to detect, such as liquid-liquid phase transformation, polymerization or dissociation. Our results suggest a novel approach to measuring viscosity in the laser-heated

diamond cell, by comparing observations of convective flow speeds in melts with numerical models. Such models are essential for describing this unique case of convection at ultra-low Rayleigh number, in which geometric controls on flow are especially pronounced. Theoretical, *ab-initio* descriptions of materials transport and mechanical properties at extremes can also assist in the collection and interpretation of motion data. Of particular interest for theoretical investigation are the viscosities of high pressure liquids, but mechanical properties of high pressure-temperature solids are also needed, for example, where melt temperatures approach bond-dissociation and diffusion-activation energies[5] and where viscoelastic[17] or rapidly-recrystallizing[4,10,16,17,42,52] states appear.

REFERENCES

[1] D. Alfè, L. Vocadlo, and G. Price, Journal of Physics-Condensed Matter **16**, S973 (2004).

[2] L. Vocadlo, "Core viscosity," in *Encyclopedia of Geomagnetism and Paleomagnetism*, edited by D. Gubbins and E. Herrero-Bervera (Springer Netherlands, 2007) p. 104.

[3] R. Boehler, Nature **363**, 534 (1993).

[4] S. Anzellini, A. Dewaele, M. Mezouar, P. Loubeyre, and G. Morard, Science **340**, 464 (2013).

[5] R. S. McWilliams, D. K. Spaulding, J. H. Eggert, P. M. Celliers, D. G. Hicks, R. F. Smith, G. W. Collins, and R. Jeanloz, Science **338**, 1330 (2012).

[6] T. Kimura, Y. Kuwayama, and T. Yagi, The Journal of Chemical Physics **140**, 074501 (2014).

[7] N. Subramanian, A. F. Goncharov, V. V. Struzhkin, M. Somayazulu, and R. J. Hemley, Proceedings of the National Academy of Sciences **108**, 6014 (2011).

[8] Q. Williams, R. Jeanloz, J. Bass, B. Svendsen, and T. J. Ahrens, Science **236**, 181 (1987).

[9]R. Boehler, N. von Bargen, and A. Chopelas, Journal of Geophysical Research: Solid Earth **95**, 21731 (1990).

[10]R. Boehler, Reviews of Geophysics **38**, 221 (2000).

[11]W. Bassett and M. Weathers, High-Pressure Research in Mineral Physics: A Volume in Honor of Syun-iti Akimoto (1987).

[12]R. S. McWilliams, D. A. Dalton, Z. Konôpková, M. F. Mahmood, and A. F. Goncharov, Proceedings of the National Academy of Sciences **112**, 7925 (2015).

[13]J. H. Eggert, D. G. Hicks, P. M. Celliers, D. K. Bradley, R. S. McWilliams, R. Jeanloz, J. E. Miller, T. R. Boehly, and G. W. Collins, Nat Phys **6**, 40 (2010).

[14]A. Belonoshko, R. Ahuja, and B. Johansson, Phys. Rev. B **61**, 11928 (2000).

[15]A. B. Belonoshko, S. I. Simak, A. E. Kochetov, B. Johansson, L. Burakovsky, and D. L. Preston, Phys. Rev. Lett. **92** (2004).

[16]A. Dewaele, M. Mezouar, N. Guignot, and P. Loubeyre, Phys. Rev. Lett. **104**, 255701 (2010).

[17]M. Ross, D. Errandonea, and R. Boehler, Phys. Rev. B **76** (2007).

[18]S. Bodea and R. Jeanloz, J. Appl. Phys. **65**, 4688 (1989).

[19]R. Jeanloz and A. Kavner, Phil. Trans. R. Soc. Lond. A **354**, 1279 (1996).

[20]M. Manga and R. Jeanloz, Geophys. Res. Lett. **23**, 1845 (1996).

[21]M. Manga and R. Jeanloz, Geoph Monog Series **101** (1998).

[22]H. Morishima and H. Yusa, J. Appl. Phys. **83**, 4572 (1998).

[23]A. Dewaele, G. Fiquet, and P. Gillet, Review of Scientific Instruments **69**, 2421 (1998).

[24]W. Panero and R. Jeanloz, J. Geophys. Res. **106**, 6493 (2001).

[25]B. Kiefer and T. S. Duffy, J. Appl. Phys. **97**, 114902 (2005).

[26]Z. Konôpková, P. Lazor, A. F. Goncharov, and V. V. Struzhkin, High Pressure Research **31** (2011).

[27]J. A. Montoya and A. F. Goncharov, J. Appl. Phys. **111**, 9 (2012).

[28]Z. M. Geballe and R. Jeanloz, J. Appl. Phys. **111**, 123518 (2012).

[29]E. S. G. Rainey, J. W. Hernlund, and A. Kavner, J. Appl. Phys. **114**, 204905 (2013).

[30]R. S. McWilliams, Z. Konôpková, and A. F. Goncharov, Physics of the Earth and Planetary Interiors **247**, 17 (2015).

[31]Z. Konôpková, R. S. McWilliams, N. Gomez-Perez, and A. F. Goncharov, Nature **534** (2016).

[724] [32]A. Zerr and R. Boehler, Science **262**, 553 (1993).

[725] [33]R. Boehler, M. Ross, and D. B. Boercker, Phys. Rev. Lett. **78**, 4589 (1997).

[726] [34]D. Errandonea, Journal of Physics and Chemistry of Solids **67**, 2017 (2006).

[727] [35]D. Errandonea, B. Schwager, R. Ditz, C. Gessmann, R. Boehler, and M. Ross, Phys. Rev.
[728] B **63**, 2104 (2001).

[729] [36]G. Shen, P. Lazor, and S. K. Saxena, Phys Chem Miner **20**, 91 (1993).

[730] [37]P. Lazor and S. K. Saxena, Phil. Trans. R. Soc. Lond. A **354**, 1307 (1996).

[731] [38]S. Japel, B. Schwager, R. Boehler, and M. Ross, Phys. Rev. Lett. **95**, 167801 (2005).

[732] [39]B. Schwager, M. Ross, S. Japel, and R. Boehler, J. Chem. Phys. **133**, 084501 (2010).

[733] [40]R. Boehler, M. Ross, P. Söderlind, and D. Boercker, Phys. Rev. Lett. **86**, 5731 (2001).

[734] [41]R. Salem, S. Matityahu, A. Melchior, M. Nikolaevsky, O. Noked, and E. Sterer, Review
[735] of Scientific Instruments **86**, 093907 (2015).

[736] [42]A. B. Belonoshko and L. S. Dubrovinsky, American Mineralogist **82**, 441 (1997).

[737] [43]C. J. Wu, P. Söderlind, J. N. Glosli, and J. E. Klepeis, Nature Materials **8**, 223 (2009).

[738] [44]A. Karandikar and R. Boehler, Phys. Rev. B **93**, 054107 (2016).

[739] [45]G. Shen and P. Lazor, Journal of Geophysical Research: Solid Earth **100**, 17699 (1995).

[740] [46]G. J. Pert, "Introductory fluid mechanics for physicists and mathematicians," (Wiley,
[741] 2013) pp. 194–196.

[742] [47]R. S. McWilliams, D. A. Dalton, M. F. Mahmood, and A. F. Goncharov, Phys. Rev. Lett.
[743] **116**, 255501 (2016).

[744] [48]E. M. Alawadhi and C. H. Amon, IEEE Transactions on Components and Packaging
[745] Technologies **26**, 116 (2003).

[746] [49]L. Yang, A. Karandikar, and R. Boehler, Review of Scientific Instruments **83**, 063905
[747] (2012).

[748] [50]J. Badro, J. Siebert, and F. Nimmo, Nature **536**, 326 (2016).

[749] [51]A. B. Belonoshko, O. LeBacq, R. Ahuja, and B. Johansson, J. Chem. Phys. **117**, 7233
[750] (2002).

[751] [52]R. Boehler, D. Santamaría-Pérez, D. Errandonea, and M. Mezouar, J. Phys.: Conf. Ser.
[752] **121**, 022018 (2008).

[753] [53]K.-I. Funakoshi, High Pressure Research **30**, 60 (2010).